

# Three dimensional localization of nanoscale battery reactions using soft X-ray tomography

Young-Sang Yu<sup>1,2</sup>, Maryam Farmand<sup>1</sup>, Chunjoong Kim<sup>2,3</sup>, Yijin Liu<sup>4</sup>, Clare P. Grey<sup>5,6</sup>, Fiona C. Strobridge<sup>5</sup>, Tolek Tyliczszak<sup>1</sup>, Rich Celestre<sup>1</sup>, Peter Denes<sup>1</sup>, John Joseph<sup>7</sup>, Harinarayan Krishnan<sup>8</sup>, Filipe R.N.C. Maia<sup>9</sup>, A. L. David Kilcoyne<sup>1</sup>, Stefano Marchesini<sup>1</sup>, Talita Perciano Costa Leite<sup>8</sup>, Tony Warwick<sup>1</sup>, Howard Padmore<sup>1</sup>, Jordi Cabana<sup>2\*</sup> and David A. Shapiro<sup>1\*</sup>

<sup>1</sup>Advanced Light Source, Lawrence Berkeley National Laboratory, Berkeley, California 94720, USA.

<sup>2</sup>Department of Chemistry, University of Illinois at Chicago, Chicago, Illinois 60607, USA.

<sup>3</sup>Department of Materials Science and Engineering, Chungnam National University, Daejeon, Chungnam 305-764, South Korea.

<sup>4</sup>Stanford Synchrotron Radiation Lightsource, SLAC National Accelerator Laboratory, Menlo Park, California 94025, USA.

<sup>5</sup>Department of Chemistry, University of Cambridge, Lensfield Road, Cambridge CB2 1EW, UK.

<sup>6</sup>Department of Chemistry, Stony Brook University, Stony Brook, New York 11794, USA.

<sup>7</sup>Engineering Division, Lawrence Berkeley National Laboratory, Berkeley, California 94720, USA.

<sup>8</sup>Computational Research Division, Lawrence Berkeley National Laboratory, Berkeley, California 94720, USA.

<sup>9</sup>Department of Cell and Molecular Biology, Uppsala University, Husargatan 3, 75124 Uppsala, Sweden.

\*E-mail: [jcabana@uic.edu](mailto:jcabana@uic.edu); [dashapiro@lbl.gov](mailto:dashapiro@lbl.gov)

Battery function is determined by the efficiency and reversibility of the electrochemical phase transformations at solid electrodes. The microscopic tools available to study the chemical states of matter with the required spatial resolution and chemical specificity are intrinsically limited when studying complex architectures by their reliance on two dimensional projections of thick material. Here, we report the development of soft X-ray ptychographic tomography, which resolves chemical states in three dimensions at 11-nm spatial resolution. We study an ensemble of nano-plates of lithium iron phosphate ( $\text{Li}_x\text{FePO}_4$ ) extracted from a battery electrode at 50% state of charge. Using a set of nanoscale tomograms, we quantify the electrochemical state and resolve phase boundaries throughout the volume of individual nanoparticles. These observations reveal multiple reaction points and intra-particle heterogeneity that highlights the importance of electrical connectivity, providing novel insight to the design of the next generation of high-performance devices.

Techniques capable of analyzing chemical states at high spatial resolution are essential for elucidating the complex phenomena at the nanoscale that underpin materials' properties. For example, battery function is determined by the efficiency and reversibility of the electrochemical phase transformations at solid electrodes, creating the need to accurately define relationships between chemistry, mechanics and morphology<sup>1,2</sup>. Conventional X-ray methods are well suited to probe bulk matter, but they are also limited in spatial resolution to a few tens of nanometers by the X-ray optics<sup>3-5</sup>. In turn, while electron-based techniques achieve high spatial resolution<sup>6-8</sup>, they are limited by multiple scattering to thin sections of material. Soft X-ray ptychography has recently narrowed the gap in spatial resolution while retaining high sensitivity to chemical states and penetration through functional volumes of matter<sup>9,10</sup>. If data is only collected along one two-dimensional (2D) projection, the analysis of complex systems becomes problematic because of the likelihood of overlapping material with differing chemical components<sup>3,4</sup>. This problem is readily solved by the use of X-ray based computed tomography, but the quantification of chemical states in three dimensions (3D) by conventional methods comes with limited spatial resolution, which is currently, at best, 30 nm<sup>3,11-13</sup>.

Here, we have combined soft X-ray ptychographic imaging and computed spectromotography to determine the three dimensional (3D) morphology and oxidation states of transition-metal cations in agglomerated cathode nano-particles of lithium iron phosphate (LiFePO<sub>4</sub>) at 11 nm 3D spatial resolution. The measured absorption at each voxel and X-ray photon energy is converted to optical density (OD) and used for computing quantitative 3D chemical composition. We investigate the complex correlation between chemical phase distribution and morphology in single nano-plates of LiFePO<sub>4</sub>, a material that epitomizes the fundamental nature of intercalation chemistry that enables electrodes for high energy density Li-ion batteries<sup>14,15</sup>. The mechanism of transformation of LiFePO<sub>4</sub> is one of the most intensely studied reactions in battery chemistry. While the reaction proceeds through a first order transition in equilibrium, under certain kinetic conditions, metastable pathways based on solid

solutions have been observed<sup>14,16-20</sup>. However, the exact conditions that determine these pathways and, more generally, how electrochemical transformations can occur within single particles of battery electrodes are still widely debated topics. Our approach enabled both direct observation of the static internal chemical structure within crystals as small as 20 nm in their smallest dimension and the evaluation of correlations of the state of charge with particle size among a statistically significant number of particles.

LiFePO<sub>4</sub> nano-plates ( $100 \times 80 \times 20 \text{ nm}^3$ ) were electrochemically delithiated until 50% of the total amount of lithium was extracted (see Method and Figs S1 and S2). The large facets correspond to the *ac* crystallographic plane with the long axis parallel to *c* (refs 10, 21). Tomographic data were collected near the Fe *L*<sub>3</sub> edge at 708.2 and 710.2 eV from over 100 harvested particles (Fig. 1a and Movie S1). The 3D resolution of 11 nm is confirmed by Fourier shell correlation and line-profiles (Figs 1b-1d and S6-S7). The energies correspond to the absorption resonances for LiFePO<sub>4</sub> (Fe<sup>2+</sup>) and FePO<sub>4</sub> (Fe<sup>3+</sup>), respectively (Fig. S4), the two thermodynamic end members in the reaction<sup>10,22-24</sup>. The oxidation states of the individual nano-plates are quantified from measurements of the OD at only two energies<sup>11,23,25</sup> because, in 3D, thickness effects, which typically require measurement of off-resonant data for normalization purposes, can be neglected owing to the constant voxel size (Method). Thus, the chemical composition is computed directly from the polar angle in the correlation plot (Figs 2a and 2b, see Method). The distribution of compositions per voxel was clearly bimodal (centers of polar angle histogram: Li<sub>0.93</sub>FePO<sub>4</sub> and Li<sub>0.02</sub>FePO<sub>4</sub>), yet the average state-of-charge (SOC) obtained by analyzing the 3D volume and independently measured 2D XAS data was 16.2% and 16.8%, respectively (Figs S9 and S10). The apparent discrepancy between this value and the 50% SOC of the electrochemical cell is addressed below. The existence of two differentiated spectroscopic components is consistent with the presence of Li<sub>α</sub>FePO<sub>4</sub> ( $\alpha \geq 0.9$ ) or Li<sub>β</sub>FePO<sub>4</sub> ( $\beta < 0.1$ ) (refs 14,26,27). Upon inspection of the resulting tomogram (Fig. 2c and Movie S1), these components were found to coexist within the same particle in several cases.

In the case of unlimited 3D spatial resolution and a binomial distribution, the upper limit of the composition error can be defined by the root-mean-square (RMS) widths of each Gaussian distribution of compositions (Fig. 2b and Method), which are  $\pm 11.3\%$  for  $\text{Li}_\alpha\text{FePO}_4$  ( $\text{Fe}^{2+}$ -rich) and  $\pm 13.9\%$  for  $\text{Li}_\beta\text{FePO}_4$  ( $\text{Fe}^{3+}$ -rich). To reduce the impact of compositional error and enhance the resolution of domains that were chemically distinct, the pixels in the 3D map (Fig. 2c) were segmented into three major components,  $>70\%$   $\text{Li}_\alpha\text{FePO}_4$  (LFP-rich),  $>70\%$   $\text{Li}_\beta\text{FePO}_4$  (FP-rich), and mixed (i.e., 30-70%  $\text{Li}_\alpha\text{FePO}_4$ , the rest being  $\text{Li}_\beta\text{FePO}_4$ ), with the segmentation threshold at 30% (Supporting Information). It is important to emphasize that this segmentation purely reflects a conservative limit of detection of a given phase, and not its specific composition (e.g.,  $\alpha$  in  $\text{Li}_\alpha\text{FePO}_4$ ). It gives a clear view of the most reliable information and is in agreement with a similarly segmented 2D XAS map with a total error of 7.4% (Fig. S11). 83 individual particles were segmented as shown in Fig. 3a (Supporting Information). The fraction of particles with smaller dimensions in the tomogram was found to be higher in comparison with a larger, and, thus, more representative population of pristine particles imaged by transmission electron microscopy (TEM, Fig. S12). Though similarly shaped, the particles presented a variety of delithiation patterns, volumes, and total composition. A histogram of particle volumes and the corresponding fraction of activated particles is shown in Fig. 3b. The average composition of all voxels in each of the morphologically segmented particles was considered to determine particle activity. Active particles showed a statistically significant level of delithiation, defined as 15-100%  $\text{Li}_\beta\text{FePO}_4$  based on a compositional error threshold ( $\sim 13\%$ ). This activity threshold should both encompass our composition error and avoid misinterpretation of particles as active due to the solubility limit of  $\text{Li}_\beta\text{FePO}_4$ . While, overall,  $\text{Li}_\alpha\text{FePO}_4$  was the major component across the range of particle volumes, 25 particles ( $30.1 \pm 5.1\%$ ) were defined as active if they had more than 15%  $\text{Li}_\beta\text{FePO}_4$ . Even with a tighter error threshold (25-100%  $\text{Li}_\beta\text{FePO}_4$ ),  $12.1 \pm 3.6\%$  particles are categorized as active. The error range

is calculated assuming a binomial distribution (active or inactive) taken at one standard deviation. Only one of the (partly) delithiated particles was found to be close to the oxidized state ( $>70\%$   $\text{Li}_\beta\text{FePO}_4$ ).

A weak tendency was observed toward an increase in the population of active particles with volume (Fig. 3b). However, the variation in *ac* facet area ( $2500 \sim 40000 \text{ nm}^2$ ) was much larger than particle thickness ( $10 \sim 30 \text{ nm}$ ). Tomography enabled the separate analysis of these particle dimensions, as shown in Fig. 3c. Interestingly, a significantly stronger dependence of the number of activated particles with facet size was found compared to overall volume. Essentially no trend was found with particle thickness, likely due to the narrow distribution of values in this dimension. The fact that particles with small facets were both systematically found to be closer to the reduced state (Fig. 3c) and oversampled in the tomogram compared to the overall population of the electrode (Fig. S12) helps explain the discrepancy between the overall SOC in the 3D image and the electrochemical cell.

Representative 3D chemical phase distributions for individual particles are shown in Fig. 4. These particles were chosen because their thickness was high enough compared to the spatial resolution to lead to insight into chemical gradients in all 3D. They also represent different degrees of delithiation. The particle showing the lowest degree of delithiation (Figs 4a-4c, overall composition  $\text{Li}_{0.89}\text{FePO}_4$ ) showed evidence of reaction primarily around the edges (blue arrows) and along one of the two large facets (red arrows) of the crystal, without clear crystallographic directionality. The existence of multiple points of reaction propagation was confirmed in a second particle at a higher delithiation state (Figs 4d-4f, overall composition  $\text{Li}_{0.81}\text{FePO}_4$ ). In this case, delithiation was also found to have occurred (red arrows) through the entire thickness of the particle. In contrast, a sharp division between single, large lithiated and delithiated domains was observed in a particle at a much higher state of delithiation (Figs 4g-4i, overall composition  $\text{Li}_{0.41}\text{FePO}_4$ ).

Our ex-situ study provides a snapshot of partly reacted states with a level of detail which serves to probe the validity of models proposed in the literature. The existence of sharp inhomogeneities within a particle is ascribed to phase separation into  $\text{Li}_\alpha\text{FePO}_4$  or  $\text{Li}_\beta\text{FePO}_4$ , where  $\alpha \gg \beta$  and  $(\alpha - \beta)$  defines the miscibility gap. The exact values of  $\alpha$  and  $\beta$  could not be extracted at the chemical resolution of our measurement, which is primarily limited by the number of energies at which tomograms are collected and our finite spatial resolution. Aside from being consistent with the thermodynamic state in  $\text{Li}_x\text{FePO}_4$  (refs 28,29), phase separation, albeit within larger individual particles than here, has been shown to prevail during slow charging in recent operando X-ray studies<sup>30,31</sup>. Models of equilibration from metastable solid solution states predict either populations of particles containing only either  $\text{Li}_\alpha\text{FePO}_4$  or  $\text{Li}_\beta\text{FePO}_4$  (ref. 19), or phase segregation along the direction of lithium diffusion, which corresponds to the thickness of the plates studied here<sup>32</sup>. Neither of these situations can explain our observations. Intra-particle heterogeneity in ex-situ conditions is also inconsistent with a domino-cascade model of delithiation, which would also lead to populations of homogeneous particles<sup>17</sup>. The population of particles with detected heterogeneity is generally larger than in other studies<sup>17,22,23</sup>. It is plausible that the higher spatial resolution achieved with ptychography in our work improved the detection of heterogeneity. It is also worth noting that the average sizes in these studies were well above 100 nm, and, thus, much larger than here. Interestingly, Brunetti *et al.* reported that mixed particles were among the smallest within the studied population<sup>33</sup>.

The existence of multiple points of reaction initiation within a particle can only be explained by a recently proposed model where surface wetting was considered in addition to coherency strain and elastic moduli within nanoparticles of similar dimensions<sup>34</sup>. Experimentally, surface wetting could result from the limited points of electronic and ionic contact between the nanocrystals and the carbon (10% w/w) and pore (electrolyte) network in

the thick porous electrodes used in a battery. These limited points for reaction initiation could also lead to gradients in composition of transient  $\text{Li}_x\text{FePO}_4$  solid solutions within a particle that would trigger immediate spinodal decomposition into two phases even under applied current, as recently predicted<sup>32</sup>. In a scenario where reaction progression is conditioned by surface wetting, the correlation between large *ac* facets and increased level of delithiation found over many particles, also suggested by others based on indirect 2D observations<sup>33</sup>, would be a trivial result of the larger probability of creating multiple points of electrical contact as facet area increases. The lack of dependence of the degree of delithiation on plate thickness is likely due the narrow distribution of available thicknesses in our sample and the compositional error of our measurement.

The chemical imaging in 3D at high resolution demonstrated here allowed us to gather new insight into scales spanning single particles to the overall state of nearly 100 particles combined, without distortions created by particle overlap. These measurements unveiled intra-particle heterogeneity and multiple reaction points, in 3D. This 3D insight allowed us to discern the effect of the dimensionality along the direction of lithium diffusion (*b* axis) from the area of the plate facet (*ac* plane), which offers a unique means to characterize materials with anisotropies in transport and volume changes during the transformation. Based on existing models of particle delithiation, this work revealed that the connectivity of a given particle to the electrical circuit, represented by the network of conductive additives and pores within the electrode architecture, critically determines the progression of the reaction. Continued development of theoretical models that incorporate the effect of electrical contacts is critical to increasing our understanding of battery electrodes. Conformal coatings that are electronically<sup>35</sup> and/or ionically<sup>36</sup> conducting would alleviate the effects of particle contact even at the smallest values of facet area, especially since small particle dimensions are needed in order to withstand the mechanical strain if any states introduce phase co-existence within a particle<sup>10</sup>.



Our demonstration of soft X-ray ptychographic tomography visualizes chemical states at a spatial resolution of 11 nm and is a powerful tool now available to chemists and materials scientists seeking insight into heterogeneous chemical distributions occurring in 3D even in nanocrystals within relatively large fields of view, thus providing the opportunity to analyze ensemble statistics. The resulting specimen thicknesses and required speeds are prohibitive for equivalent, high spatial resolution techniques in electron microscopy, making it an ideal complement to uncover phenomena at multiple scales in one measurement. This multiscale insight is critical to accurately defining the properties of functional materials in realistic architectures such as batteries.

## Methods

**Synthesis of  $\text{Li}_x\text{FePO}_4$  ( $x \sim 0.5$ ) nano-plates.** Plate-shaped  $\text{LiFePO}_4$  were synthesized using a previously reported solvothermal method<sup>10,21</sup>.  $\text{H}_3\text{PO}_4$  and  $\text{LiOH}\cdot\text{H}_2\text{O}$  were dissolved in ethylene glycol at 50 °C, followed by addition of  $\text{FeSO}_4\cdot 7\text{H}_2\text{O}$ , for a total 1:1.5:2.7 molar ratio. After stirring for 30 min, the mixture was heated at 180 °C for 10 hours. In order to achieve good conductivity,  $\text{LiFePO}_4$  nano-plates were carbon coated by mixing with 20 wt % of sucrose and then carbonizing at 650 °C for 3 hours in Ar atmosphere<sup>10,21</sup>. In order to evaluate the macroscopic electrochemical properties of the oxide and prepare the specific state-of-charge (~ 50 %), composite electrode films were fabricated by mixing the pristine oxide with acetylene black and polyvinylidene difluoride (PVDF) in a 80 : 10 : 10 ratio in N-methylpyrrolidone. The resulting slurry was cast onto a pre-weighed Al foil disk, dried at room temperature, followed by a heat treatment of 120 °C under vacuum. The composite electrodes were assembled in 2032 coin cells using lithium foil as both counter and pseudo-reference electrode, and Celgard 2400 separator soaked in a 45 : 55 mixture of ethylenecarbonate and dimethyl carbonate containing 1 M  $\text{LiPF}_6$  as electrolyte. All cell assembly and sample manipulation was performed in an Ar-filled glovebox. A Bio-Logic VMP3 potentiostat/galvanostat were used to carry out all electrochemical experiments in galvanostatic mode, at C/10 rate. Capacity at the first discharge of the preliminary cell are in good agreements with the literatures ( $156 \text{ mAh}\cdot\text{g}^{-1}$ ), showing that almost all particles were involved in the electrochemical reaction (Fig. S1). The half-charged cell (~ 50% state-of-charge) for the imaging experiments was stopped at to  $78 \text{ mAh}\cdot\text{g}^{-1}$  (Fig. S1).

**Soft X-ray ptychographic microscope.** Soft X-ray ptychographic microscopy measurements were performed at the bending magnet beamline (5.3.2.1) at the Advanced Light Source (ALS), Lawrence Berkeley National Laboratory<sup>9,10</sup>. Ptychographic measurements utilized a 100 nm outer zone width Fresnel zone plate for illumination and proceeded with a square scan grid of 70 nm steps. Diffraction patterns from 200 ms exposure were directly recorded on a custom fast readout CCD with the 5- $\mu$ m-thick Si<sub>3</sub>N<sub>4</sub> attenuator to expand the dynamic range (Fig. S2). The diffraction data were reconstructed by 500 iterations of an implementation of the RAAR algorithm<sup>37</sup>. Incoherent background noise was eliminated through the implementation of a background retrieval algorithm<sup>9</sup>. All data processing, including ptychographic reconstruction, and background retrieval were performed using standard methods available in the SHARP-CAMERA software package with parallel computation (<http://camera.lbl.gov>, ref. 38). The resolution of the individual 2D projection is calculated by Fourier ring correlation (FRC) to be 10 nm ( $\frac{1}{2}$  bit threshold, ref. 39) at 708.2 eV (see Fig. S5 and Supporting Information).

**Registration of the rotation axis.** Aligning the 2D projections of a tomographic tilt series to a common rotation axis (not necessarily the real rotation axis) with sub-pixel resolution is essential to achieve a good quality 3D reconstruction. In order to achieve sub-pixel-precision, we have developed an iterative registration method with intensity-based automatic image alignments. To set the common rotation axis, the projections were first roughly aligned using an alignment feature only with translations of pixel size. The alignment features in all roughly aligned projections were close to the common rotation axis, but there still exist huge misalignments owing to inaccuracy of human interactions and tilting of each projection. We then reconstructed the 3D volume from the first aligned tomographic tilt series and computed 2D projections of the 3D volume according to the tomographic tilt angles. These computed 2D projections were used as reference images for second alignments. The second alignment was performed with intensity-based automatic image registration, which is an iterative process

brings the misaligned image (2D projections of the tomographic tilt series) into alignment with the reference image (computed 2D projections). The process was performed following non-reflective similarity transformations (consisting of translation, rotation, and scale) to determine the specific image transformation matrix that is applied to the moving image with bilinear interpolation. The same procedures were repeated until the aligned projections were self-consistent.

**Tomographic reconstruction.** Tomographic imaging proceeded from a series of 158 two-dimensional (2D) projections of the sample ODs recorded over a wide angular range from  $-80^\circ$  to  $+77^\circ$ . After the image registration (see Supporting Information), the OD volumes at 708.2 and 710.2 eV (Fig. 1a), with voxel size of  $6.7 \times 6.7 \times 6.7 \text{ nm}^3$ , were reconstructed using the algebraic reconstruction technique (ART)<sup>40</sup>. The 3D resolution is confirmed by Fourier shell correlation (FSC) of the OD volume at 708.2 eV and indicates a 3D spatial resolution around 11 nm (see Fig. 1b and Supporting Information). This value is confirmed by line-cuts through the volume, shown in Figs 1c and 1d.

**Chemical phase quantification.** The OD volumes at 708.2 and 710.2 e V were used for estimating quantitative chemical information (e.g. the oxidation state of iron in  $\text{Li}_x\text{FePO}_4$ ) at each voxel. From the standard spectra of the discharged  $\text{Li}_\alpha\text{FePO}_4$  (majority  $\text{Fe}^{2+}$ ) and charged  $\text{Li}_\beta\text{FePO}_4$  (majority  $\text{Fe}^{3+}$ ), the relative absorption intensity ( $I_{E1,LFP}$ ,  $I_{E1,FP}$ ,  $I_{E2,LFP}$ , and  $I_{E2,FP}$ ) at specific energy ( $E_1$  and  $E_2$ ) were acquired (Fig. S4). Since, the amount of the absorption at a certain energy is linearly proportional to the relative amount of species with different iron oxidation states, the chemical concentration of  $\text{Li}_\alpha\text{FePO}_4$  ( $C_{LFP}$ ) and  $\text{Li}_\beta\text{FePO}_4$  ( $C_{FP}$ ) at each voxel can be calculated by the relation:

$$\begin{pmatrix} OD_{E1} - OD_{pre-edge} \\ OD_{E2} - OD_{pre-edge} \end{pmatrix} = \begin{pmatrix} I_{E1,LFP} & I_{E1,FP} \\ I_{E2,LFP} & I_{E2,FP} \end{pmatrix} \begin{pmatrix} C_{LFP} \\ C_{FP} \end{pmatrix}$$

where  $OD_{E1}$ ,  $OD_{E2}$ , and  $OD_{pre-edge}$  indicate the single voxel OD at  $E_1$ ,  $E_2$ , and pre-edge region, respectively. While normalization of all ODs with  $OD_{pre-edge}$  can maximize the chemical contrast, because  $OD_{pre-edge}$  is proportional to pure mass thickness without chemical contrast, the OD at pre-edge region was not clear enough to reconstruct 3D volume and negligible compared with ODs at 708.2 and 710.2 eV (Fig. S8). Since the concentration of each chemical phase,  $\text{LiFePO}_4$  ( $\text{Fe}^{2+}$ ) and charged  $\text{FePO}_4$  ( $\text{Fe}^{3+}$ ), can be expressed as linear equations corresponding to the OD volumes at 708.2 and 710.2 eV, the polar angle in the correlation plot is a function of the relative compositions of two major elements for the corresponding voxel (Fig. 2b). As a result, the 3D distribution of Fe oxidation state can be retrieved quantitatively (Fig. 2c). The fidelity of the 3D chemical map obtained in this way is verified by projecting the calculated volume along the  $z$ -axis and comparing with a map obtained by a linear combination fit of the reference spectra to independently measured 2D XAS data across the full spectrum of the same sample (Figs S10 and S11). The accuracy of the chemical map from 2D XAS data is represented by  $R$ -factor which is less than 0.15 in 94.64% of pixels (see Fig. S9 and Supporting Information).

## References

- 1 Whittingham, M. S. Ultimate limits to intercalation reactions for lithium batteries. *Chem. Rev.* **114**, 11414-11443 (2014).
- 2 Whittingham, M. S. Lithium batteries and cathode materials. *Chem. Rev.* **104**, 4271-4302 (2004).
- 3 Miao, J., Ishikawa, T., Robinson, I. K. & Murnane, M. M. Beyond crystallography: Diffractive imaging using coherent x-ray light sources. *Science* **348**, 530-535 (2015).
- 4 Sakdinawat, A. & Attwood, D. Nanoscale X-ray imaging. *Nature Photon.* **4**, 840-848 (2010).
- 5 Chao, W., Harteneck, B. D., Liddle, J. A., Anderson, E. H. & Attwood, D. T. Soft X-ray microscopy at a spatial resolution better than 15nm. *Nature* **435**, 1210-1213 (2005).
- 6 Pennycook, S. J. & Boatner, L. A. Chemically sensitive structure-imaging with a scanning transmission electron microscope. *Nature* **336**, 565-567 (1988).
- 7 Browning, N. D., Chisholm, M. F. & Pennycook, S. J. Atomic-resolution chemical analysis using a scanning transmission electron microscope. *Nature* **366**, 143-146 (1993).
- 8 Batson, P. E., Dellby, N. & Krivanek, O. L. Sub-angstrom resolution using aberration corrected electron optics. *Nature* **418**, 617-620 (2002).
- 9 Shapiro, D. A. *et al.* Chemical composition mapping with nanometre resolution by soft X-ray microscopy. *Nature Photon.* **8**, 765-769 (2014).
- 10 Yu, Y.-S. *et al.* Dependence on crystal size of the nanoscale chemical phase distribution and fracture in  $\text{Li}_x\text{FePO}_4$ . *Nano Lett.* **15**, 4282-4288 (2015).
- 11 Johansson, G. A., Tyliszczak, T., Mitchell, G. E., Keefe, M. H. & Hitchcock, A. P. Three-dimensional chemical mapping by scanning transmission X-ray spectromicroscopy. *J. Synchrotron Radiat.* **14**, 395-402 (2007).
- 12 Meirer, F. *et al.* Three-dimensional imaging of chemical phase transformations at the nanoscale with full-field transmission X-ray microscopy. *J. Synchrotron Radiat.* **18**, 773-781 (2011).
- 13 Yang, F. *et al.* Nanoscale morphological and chemical changes of high voltage lithium-manganese rich nmc composite cathodes with cycling. *Nano Lett.* **14**, 4334-4341 (2014).
- 14 Padhi, A. K., Nanjundaswamy, K. S. & Goodenough, J. B. Phospho-olivines as positive-electrode materials for rechargeable lithium batteries. *J. Electrochem. Soc.* **144**, 1188-1194 (1997).
- 15 Zaghib, K., Mauger, A. & Julien, C. M. Overview of olivines in lithium batteries for green transportation and energy storage. *J. Solid State Electrochem.* **16**, 835-845 (2012).
- 16 Laffont, L. *et al.* Study of the  $\text{LiFePO}_4/\text{FePO}_4$  two-phase system by high-resolution electron energy loss spectroscopy. *Chem. Mater.* **18**, 5520-5529 (2006).
- 17 Delmas, C., Maccario, M., Croguennec, L., Le Cras, F. & Weill, F. Lithium deintercalation in  $\text{LiFePO}_4$  nanoparticles via a domino-cascade model. *Nature Mater.* **7**, 665-671 (2008).
- 18 Andersson, A. S. & Thomas, J. O. The source of first-cycle capacity loss in  $\text{LiFePO}_4$ . *J. Power Sources* **97-98**, 498-502 (2001).
- 19 Malik, R., Zhou, F. & Ceder, G. Kinetics of non-equilibrium lithium incorporation in  $\text{LiFePO}_4$ . *Nature Mater.* **10**, 587-590 (2011).
- 20 Liu, H. *et al.* Capturing metastable structures during high-rate cycling of  $\text{LiFePO}_4$  nanoparticle electrodes. *Science* **344**, 1252817 (2014).

- 21 Wang, L. *et al.* Crystal orientation tuning of LiFePO<sub>4</sub> nanoplates for high rate lithium battery cathode materials. *Nano Lett.* **12**, 5632-5636 (2012).
- 22 Chueh, W. C. *et al.* Intercalation pathway in many-particle LiFePO<sub>4</sub> electrode revealed by nanoscale state-of-charge mapping. *Nano Lett.* **13**, 866-872 (2013).
- 23 Li, Y. *et al.* Dichotomy in the lithiation pathway of ellipsoidal and platelet LiFePO<sub>4</sub> particles revealed through nanoscale operando state-of-charge imaging. *Adv. Funct. Mater.* **25**, 3677-3687 (2015).
- 24 Li, Y. *et al.* Current-induced transition from particle-by-particle to concurrent intercalation in phase-separating battery electrodes. *Nature Mater.* **13**, 1149-1156 (2014).
- 25 Kao, T. L. *et al.* Nanoscale elemental sensitivity study of Nd<sub>2</sub>Fe<sub>14</sub>B using absorption correlation tomography. *Microsc. Res. Tech.* **76**, 1112-1117 (2013).
- 26 Yamada, A. *et al.* Room-temperature miscibility gap in Li<sub>x</sub>FePO<sub>4</sub>. *Nature Mater.* **5**, 357-360 (2006).
- 27 Wagemaker, M. *et al.* Dynamic solubility limits in nanosized olivine LiFePO<sub>4</sub>. *J. Am. Chem. Soc.* **133**, 10222-10228 (2011).
- 28 Delacourt, C., Poizot, P., Tarascon, J.-M. & Masquelier, C. The existence of a temperature-driven solid solution in Li<sub>x</sub>FePO<sub>4</sub> for  $0 \leq x \leq 1$ . *Nature Materials* **4**, 254-260 (2005).
- 29 Zhou, F., Maxisch, T., & Ceder, G. Configurational electronic entropy and the phase diagram of mixed-valence oxides: the case of Li<sub>x</sub>FePO<sub>4</sub>. *Phys. Rev. Lett.* **97**, 155704 (2006).
- 30 Zhang, X., Van Hulzen, M., Singh, D. P., Brownrigg, A., Wright, J. P., Van Dijk, N. H. & Wagemaker, M. Direct view on the phase evolution in individual LiFePO<sub>4</sub> nanoparticles during Li-ion battery cycling. *Nat. Commun.* **6**, 8333 (2015).
- 31 Lim, J. *et al.* Origin and hysteresis of lithium compositional spatiodynamics within battery primary particles. *Science* **353**, 566-571 (2016).
- 32 Abdellahi, A., Akyildiz, O., Malik, R., Thorntonc, K. & Ceder, G. The thermodynamic stability of intermediate solid solutions in LiFePO<sub>4</sub> nanoparticles. *J. Mater. Chem. A* **4**, 5436-5447 (2016).
- 33 Brunetti, G., Robert, D., Bayle-Guillemaud, P., Rouvière, J. L., Rauch, E. F., Martin, J. F., Colin, J. F., Bertin, F. & Cayron, C. Confirmation of the domino-cascade model by LiFePO<sub>4</sub>/FePO<sub>4</sub> precession electron diffraction. *Chem. Mater.* **23**, 4515-4524 (2011).
- 34 Welland, M. J., Karpeyev, D., O'Connor, D. T. & Heinonen, O. Miscibility gap closure, interface morphology, and phase microstructure of 3D Li<sub>x</sub>FePO<sub>4</sub> nanoparticles from surface wetting and coherency strain. *ACS Nano* **9**, 9757-9771 (2015).
- 35 Raveta, N., Chouinarda, Y., Magnanb, J.F., Besnerb, S., Gauthiera, M. & Armanda M. Electroactivity of natural and synthetic triphylite. *J. Power Sources* **97-98**, 503-507 (2001).
- 36 Kang, B. & Ceder, G. Battery materials for ultrafast charging and discharging. *Nature* **458**, 190-193 (2009).
- 37 Luke, D. R. Relaxed averaged alternating reflections for diffraction imaging. *Inverse Probl.* **21**, 37 (2005).
- 38 Marchesini, S. *et al.*, SHARP: a distributed, GPU-based ptychographic solver, arXiv:1602.01448 (2016).
- 39 van Heel, M. & Schatz, M. Fourier shell correlation threshold criteria. *J. Struct. Biol.* **151**, 250-262 (2005).
- 40 Gordon, R., Bender, R. & Herman, G. T. Algebraic Reconstruction Techniques (ART) for three-dimensional electron microscopy and X-ray photography. *J. Theor. Biol.* **29**, 471-481 (1970).

**Acknowledgments.**

Soft X-ray ptychographic microscopy was carried out at beamline 5.3.2.1 at the Advanced Light Source. The Advanced Light Source is supported by the Director, Office of Science, Office of Basic Energy Sciences, of the U.S. Department of Energy under Contract No. DE-AC02-05CH11231. This work was supported as part of the NorthEast Center for Chemical Energy Storage, an Energy Frontier Research Center funded by the U.S. Department of Energy, Office of Science, Office of Basic Energy Sciences under Award Number DE-SC0012583. This work is partially supported by the Center for Applied Mathematics for Energy Research Applications (CAMERA), which is a partnership between Basic Energy Sciences (BES) and Advanced Scientific Computing Research (ASRC) at the U.S Department of Energy.

**Author contributions:**

Y.-S.Y., C.K., J.C., and D.A.S. conceived of and planned the experiment. D.A.S., T.T., R.C., P.D., J.J, H.K., F.R.N.C.M., A.L.D.K., T.P.C.L., T.W., Y.-S.Y., and H.P. developed experimental techniques, software and equipment. D.A.S. and S.M. developed ptychographic reconstruction codes. Y.-S.Y., C.K., F.C.S., and C.P.G. prepared the samples. Y.-S.Y., M.F., and D.A.S. carried out the ptychographic microscopy measurements. Y.-S.Y., Y.L., and D.A.S. performed post-experiment data analysis, and Y.-S.Y., Y.L., C.K., D.A.S, and J.C. established the interpretation of the chemical maps. Y.-S.Y., C.K., J.C., and D.A.S. prepared the manuscript, which incorporates critical input from all authors.



**Figure 1| Results of tomographic reconstruction.** **a**, Reconstructed three dimensional (3D) optical density volumes at 708.2 (left) and 710.2 eV (right). The size of reconstructed voxels is  $6.7 \times 6.7 \times 6.7 \text{ nm}^3$ . **b**, Resolution estimation of the 3D volume at 708.2 eV in **(a)** by Fourier shell correlation (FSC, blue solid line with scatter) with 1/2-bit (red solid line) and 0.5 (magenta dashed-line) threshold criteria. **c**, Representative cross-section of the tomogram at 708.2 eV along the highest resolution plane ( $xy$ ). The slice of the same position at 710.2 eV is shown in Fig. S6. The positions of the slices are marked as red (cutting along  $xy$  plane) and blue (cutting along  $xz$  plane) arrows in **(a)**. The resultant cross-sections onto the lower resolution plane ( $xz$  plane) at both 708.2 and 710.2 eV are shown in Fig. S7. **d**, Line profile indicated by the red arrow in **(c)**. Black-dashed lines are guides for 10-90% resolution criteria.

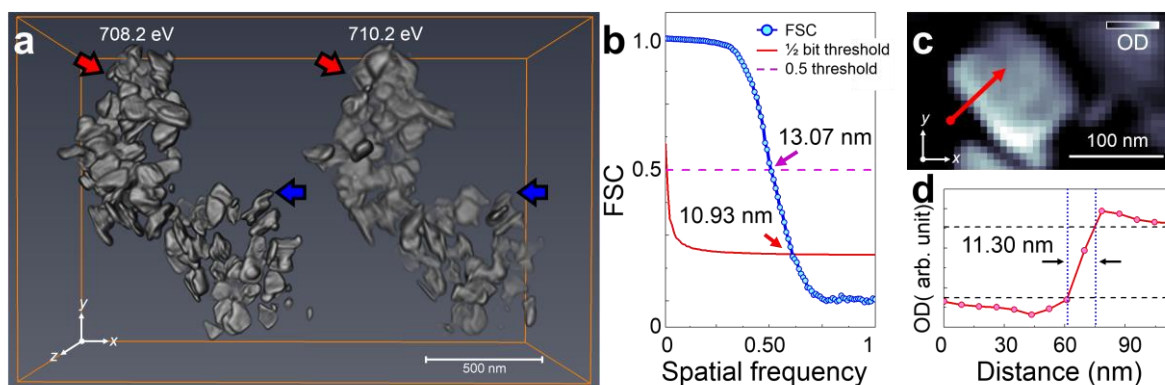


**Figure 2| Three dimensional (3D) chemical state mapping.** **a**, Correlative distribution plots between the optical densities (ODs) of each voxel at 708.2 and 710.2 eV. **b**, Histogram plot of the polar angles of the data points in (a). The y axis is expressed as a logarithmic scale for better visibility. The plot can be fitted with summation (black solid line) of two Gaussian distributions which are centered on low (magenta solid line, 27.48°) and high (Cyan solid line, 65.0°) polar angles correspond to  $\text{Li}_{0.93}\text{FePO}_4$  and  $\text{Li}_{0.02}\text{FePO}_4$ , respectively. **c**, 3D chemical map (left) and its segmentation into three chemical phase groups (right). The presence of the  $\text{Li}_\alpha\text{FePO}_4$  (majority  $\text{Fe}^{2+}$ , LFP) and charged  $\text{Li}_\beta\text{FePO}_4$  (majority  $\text{Fe}^{3+}$ , FP) were assigned colors red and blue, respectively (left). The voxels were separated into three distinct groups, indicating chemical phase group of each voxel, according to the polar angle. The red, green, and blue areas indicate LFP-rich (>70%  $\text{Li}_\alpha\text{FePO}_4$ ), FP-rich (>70%  $\text{Li}_\beta\text{FePO}_4$ ), and Mixed (30-70%  $\text{Li}_\alpha\text{FePO}_4$ , the rest being  $\text{Li}_\beta\text{FePO}_4$ ) domains, respectively. The shading colors in (a, b) indicate the criteria for chemical segmentation.

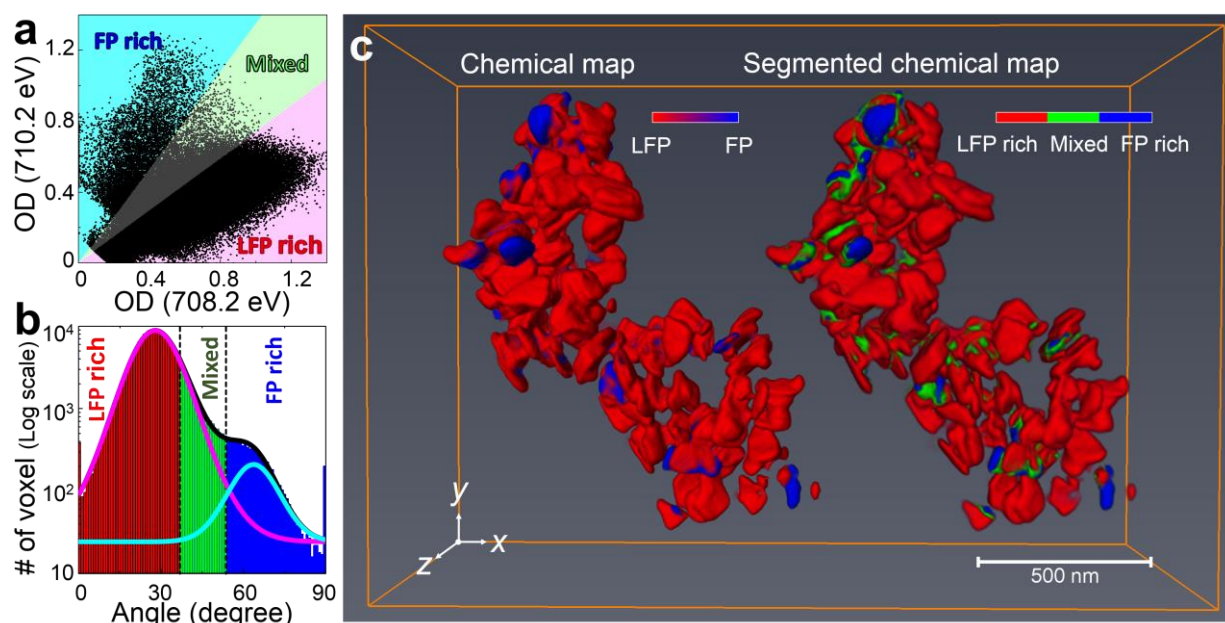


**Figure 3| Activeness of each particle. a,** Voxel segmentation to define individual particles. **b,** Volume distributions (black solid line with scatter) of individual particles shown in Fig. 2 and the fraction (bar plot) of inactive (magenta bar, <15% of  $\text{Li}_\beta\text{FePO}_4$ ) and active (olive bar, 15-100% of  $\text{Li}_\beta\text{FePO}_4$ ) particles as a function of particle volume with an increments of 200 voxels' volume. Averaged particle volume in each range also shown. Each voxel has a volume of  $6.7 \times 6.7 \times 6.7 \text{ nm}^3$ . The experimental error bars are calculated assuming a binomial distribution (active or inactive) taken at one standard deviation. **c,** Compositional analysis based on the dimensions of each plate, comparing the facet area with thickness. The optical densities (ODs) of voxels along the particle thickness direction were averaged out across whole large facet. The thickness of the particle was calculated by the full-width-half-maxima of the averaged OD. The bar plots have the same color definition as (b).

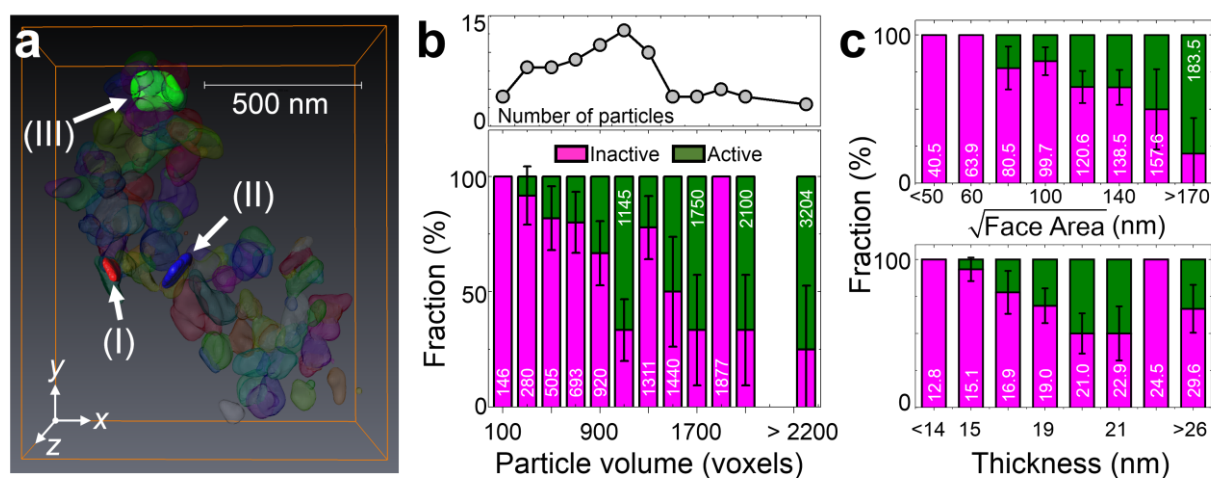
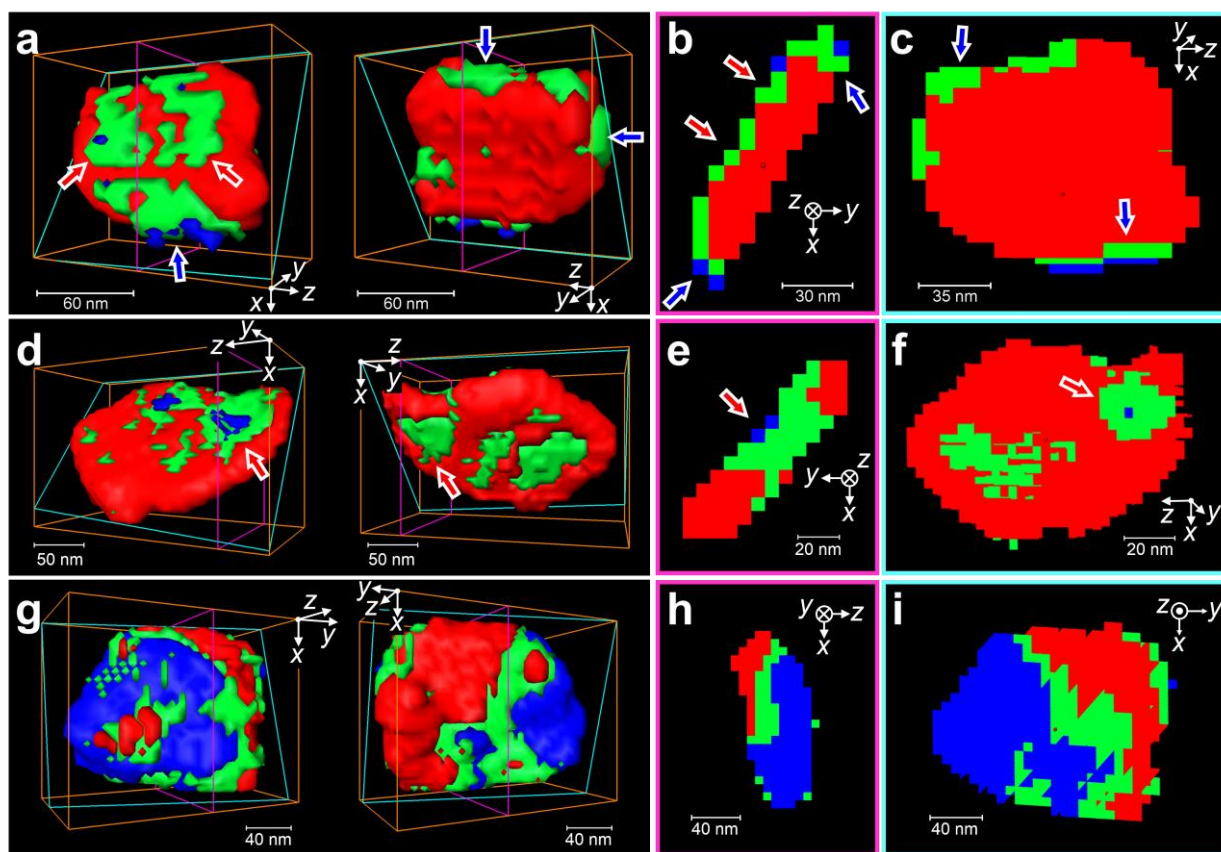


**Figure 4| Representative three dimensional (3D) chemical phase distribution of individual particle.** **a,d,g**, Front (left) and backside (right) views of isosurface of three chemical components. Cross-sectional views along the thickness direction (**b, e, h**) and along the large face (**c, f, i**), respectively. The cross-section planes are indicated as magenta and cyan colored boxes in 3D isosurface plots. The red, green, and blue indicate LFP-rich, mixed, and FP-rich voxels, respectively. The positions of each particle are noted as (I), (II), and (III) in Fig. 3a for (**a**), (**d**) and (**g**), respectively.



## Supplementary Text

**Fourier ring correlation (FRC).** For the FRC in Fig. S5, the diffraction data at  $0^\circ$  were divided into two separate subsets by selecting every other measurement, which were then reconstructed as independent OD images of the same object<sup>1</sup>. The actual resolution should be somewhat higher as the FRC reduces the signal-to-noise ratio of the data by a factor of two.

**Fourier shell correlation (FSC).** In order to calculate the FSC, the 158 OD projections at each X-ray energy were divided into two separate subsets corresponding to even and odd tomographic tilt angles ( $\theta$ ), and then were reconstructed as an independent OD volume of the same object. The FSC of the lower contrast OD volume at 710.2 eV presents a 3D resolution of 12 - 14 nm (Figs S6 and S7). Note that the actual resolution should be somewhat higher as the FRC reduces the signal-to-noise ratio of the data by a factor of two. These 3D resolutions are close to the theoretical resolution limit of 10 nm expected from the angular sampling of the sample diameter (i.e. approximately  $0.5\ \mu\text{m}$  in this case) based on the Crowther–DeRosier–Klug formula<sup>2</sup>.

**Quantitative 2D chemical phase map with X-ray absorption spectra:** A series OD images of the  $\text{Li}_x\text{FePO}_4$  crystals across the Fe  $L_3$  absorption edge were recorded by Soft X-ray ptychographic microscopy at 5.3.2.1 of the Advanced Light Source<sup>3,4</sup>. After ptychographic image reconstructions and pre-processing (e.g. image registration, background subtractions, reduction of sparkling noise, etc.), single pixel X-ray absorption spectra (XAS) were produced by integrating the OD across the energy. Reference spectra for pristine  $\text{LiFePO}_4$  and chemically delithiated  $\text{FePO}_4$  crystals were extracted from averaged linescans with energy step of 0.2 eV (Fig. S4). All single pixel spectra were fit by a linear combination (LC) of standard spectra (Fig. S9) of  $\text{LiFePO}_4$  and  $\text{FePO}_4$ . The quality of each LC fit can be checked with the  $R$ -factor map

(Fig. S9) defined as,  $R = \sum (\text{data-fit})^2 / \sum (\text{data})^2$  (ref. 4). 94.64% of pixels were fit with  $R$ -factors less than 0.15. Pixels showing poor signal-to-noise ratios were filtered out by a lower bound of the  $R$ -factor. Representative single pixel XAS and the corresponding fits are presented in Fig. S9c.

**Segmentation of chemical phases:** To reduce the error in the quantitative chemical map from two energy analysis, the chemical phases were segmented into three major components, such as LFP-rich, mixed, and FP-rich with the segmentation threshold (Fig. S11). According to the segmentation threshold ( $X$ ), each chemical component was defined as:

LFP-rich:  $>(100-X)\%$  of  $\text{Li}_\alpha\text{FePO}_4$  ( $\alpha \geq 0.9$ );

Mixed:  $(100-X) \sim X\%$   $\text{Li}_\alpha\text{FePO}_4$ , the rest being  $\text{Li}_\beta\text{FePO}_4$  ( $\beta < 0.1$ );

FP-rich:  $>(100-X)\%$  of  $\text{Li}_\beta\text{FePO}_4$  ( $\beta < 0.1$ ).

This segmentation, with  $X = 30$ , gives a clear view of the most reliable information and is in agreement with a similarly segmented 2D XAS map with a total error of 7.4%.

**Segmentation of individual particles:** Dark and bright voxels in the 3D reconstructed OD volumes correspond to a region of weak absorption (e.g. porosity, carbon black, and polymer binder) and  $\text{Li}_x\text{FePO}_4$  particles, respectively. To enhance the contrast, the ODs at 708.2 and 710.2 eV were averaged for representing the total iron content in the volume. The strong contrast in the OD volume was converted to level-based binary slices. The small features in the binarized slices were filled or removed before segmentation for avoiding over/under-segmentation. We computed distance maps from binary images and created center positions for each segment from maxima regions of the distance map, then applied a 3D watershed algorithm<sup>5</sup>. Due to the weak contrast between proximate particles, the watershed algorithm caused inaccurate segmentation in some cases. To overcome these problems, we have

introduced a criterion based on knowledge of the particle shape (i.e.  $\text{LiFePO}_4$  has a plate-like shape in our case) and combined/separated to compensate for the inaccurate segmentation. Owing to unclear boundaries between some particles, a total of 27 particle bunches were not segmented, and the 83 individual particles were analyzed.

**Figure S1.** Galvanostatic charge/discharge profiles of the first (blue solid line) and second (black solid line) cycles of  $\text{LiFePO}_4$  nano-plates under normal cycling conditions (room temperature, C/10 rate).  $\text{Li}_x\text{FePO}_4$  ( $x \sim 0.5$ ) nano-plates were harvested from the separate half-charged coin-cell (red solid line), that was interrupted at a capacity of  $78 \text{ mAh}\cdot\text{g}^{-1}$  (red solid cycle) during the first charge sequence.

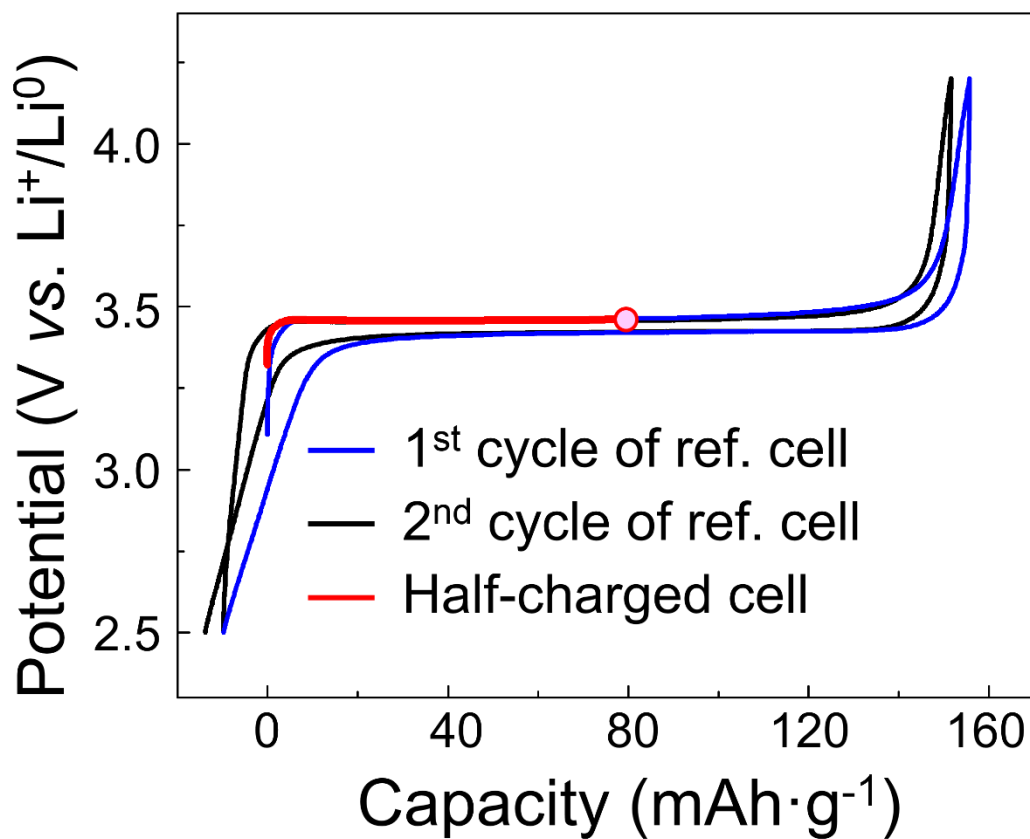




**Figure S2.** Representative scanning electron microscopy (SEM) image of  $\text{Li}_x\text{FePO}_4$ .

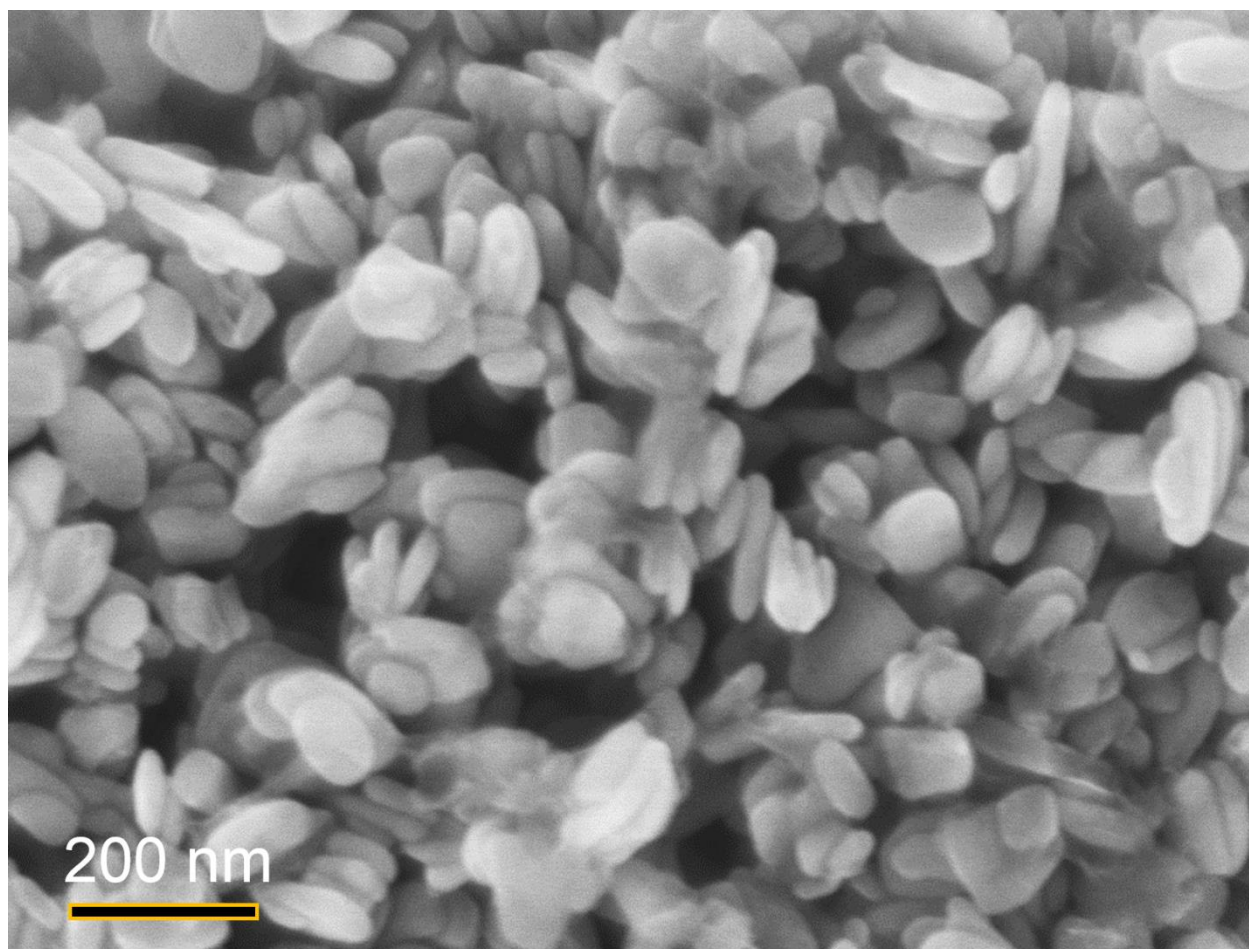


**Figure S3.** Diagram of soft X-ray ptychographic microscopy. A monochromatic and coherent soft X-ray beam is focused onto the sample using a 100 nm outer-zone-width Fresnel zone plate (FZP). An order-sorting aperture (OSA) filters out higher-order diffraction. With mechanical raster motions of the FZP, the focused X-ray is scanned onto the sample to collect a series of diffraction patterns with 70 nm step to ensure overlap of the probed areas. Diffraction patterns are recorded on an X-ray charge-coupled device (CCD) positioned 80 mm downstream of the sample. To expand the dynamic range of the CCD, the central portions of the diffraction data are attenuated by the 5- $\mu\text{m}$ -thick  $\text{Si}_3\text{N}_4$  attenuator. In order to record 2-dimensional images at various angular positions of the sample with respect to the X-ray beam, the sample is placed on a stage with high precision  $x$ ,  $y$ ,  $z$ , and  $\theta$  (tomographic tilt angles) stage, which was stabilized by an optical interferometry (blue and green arrows).

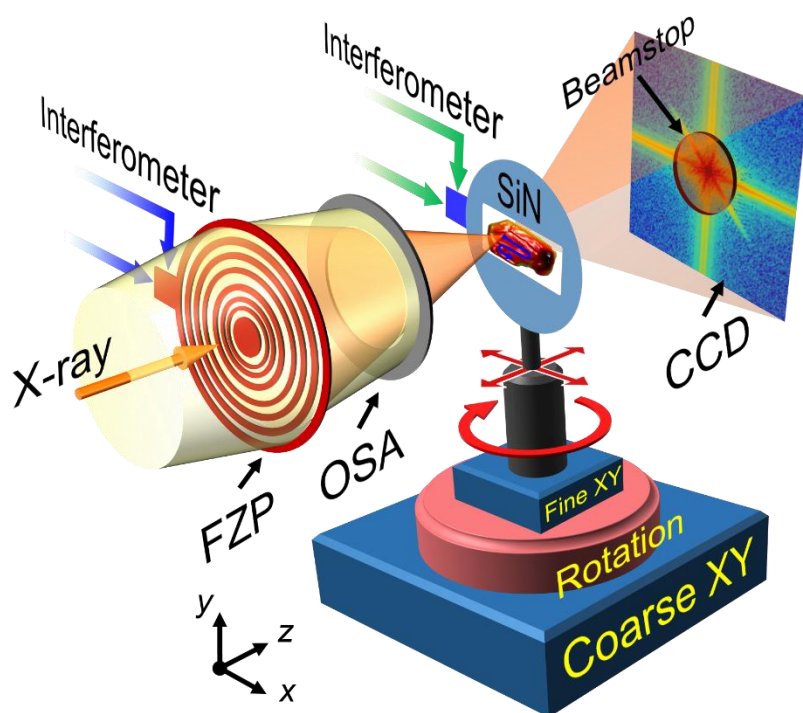


**Figure S4.** Fe  $L_3$  X-ray absorption reference spectra taken from pristine LiFePO<sub>4</sub> nanoplates and FePO<sub>4</sub> produced by chemical delithiation. To reduce the noise, over 15 spectra are averaged. Each spectrum was collected by linescan mode in conventional scanning X-ray microscopes (STXM) with energy step of 0.2 eV. The absorption at the specific energies ( $E_1$  and  $E_2$ ) are defined as  $I_{E1,LFP}$ ,  $I_{E1,FP}$ ,  $I_{E2,LFP}$ , and  $I_{E2,FP}$ . The pure mass thickness term in the reference spectra is defined as  $I_{pre-edge}$ .

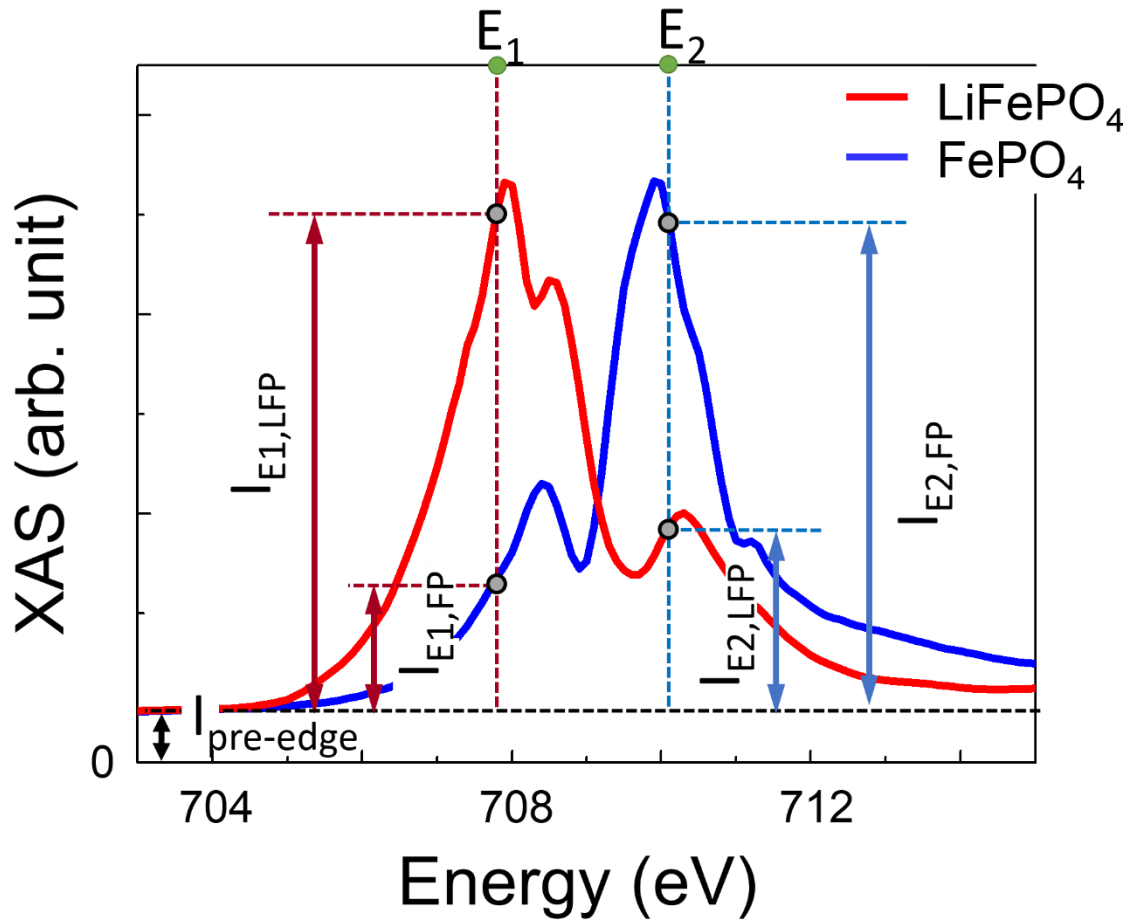


**Figure S5. a**, Phychographic reconstructions of two-dimensional (2D) optical density (OD) at specific tilt angles ( $\theta$ ) as noted. The size of reconstructed pixels is  $6.7 \times 6.7 \text{ nm}^2$ . **b**, Resolution estimation of the image at  $0^\circ$  in (a) by Fourier ring correlation (FRC, blue solid line with scatter) with 1/2-bit (red solid line) and 0.5 (magenta dashed-line) threshold criteria.

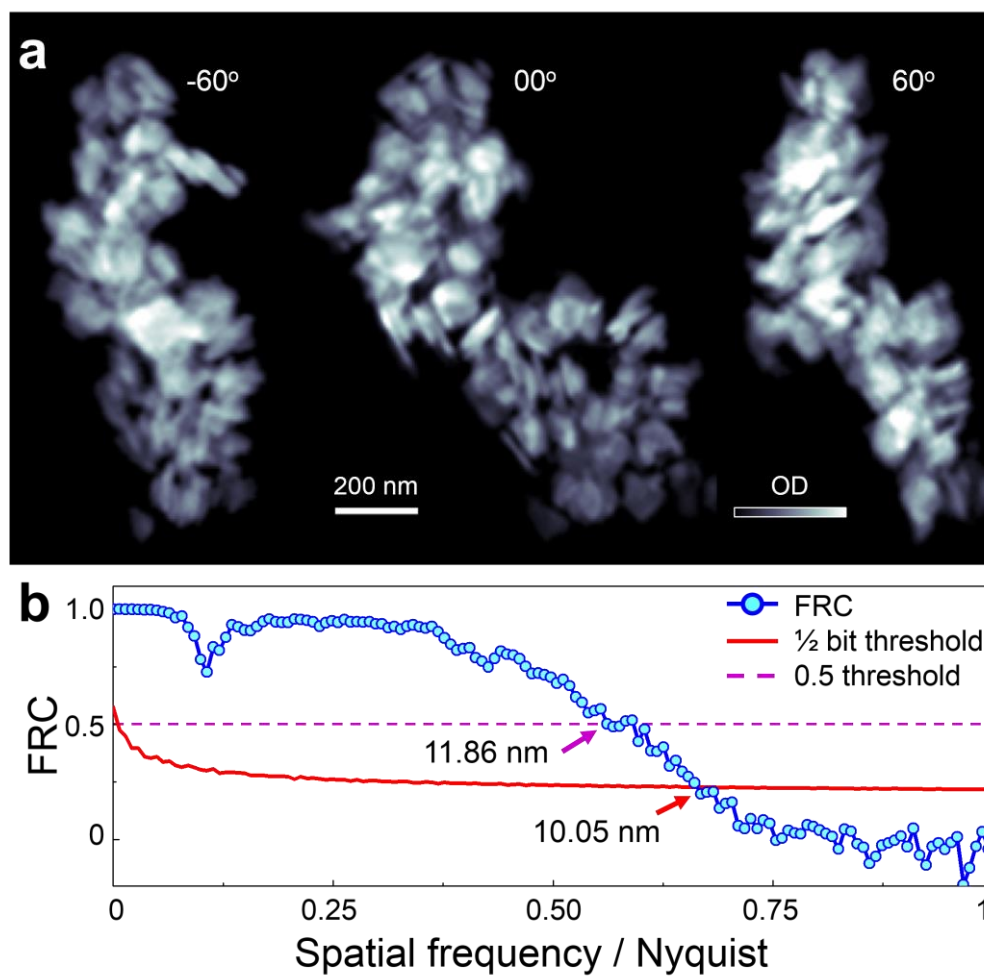


**Figure S6. a**, Resolution of the three-dimensional (3D) optical density (OD) volume at 710.2 eV in Fig. 1 by Fourier shell correlation (FSC, blue solid line with scatter) with 1/2-bit (red solid line) and 0.5 (magenta dashed-line) threshold criteria. **b**, Representative cross-section of the tomogram at 710.2 eV along the highest resolution plane ( $xy$ ). The positions of the slices are marked as red arrows in Fig. 1a. **c**, Line profile indicated by the red arrow in **b**. Black-dashed lines are guides for 10-90% resolution criteria.

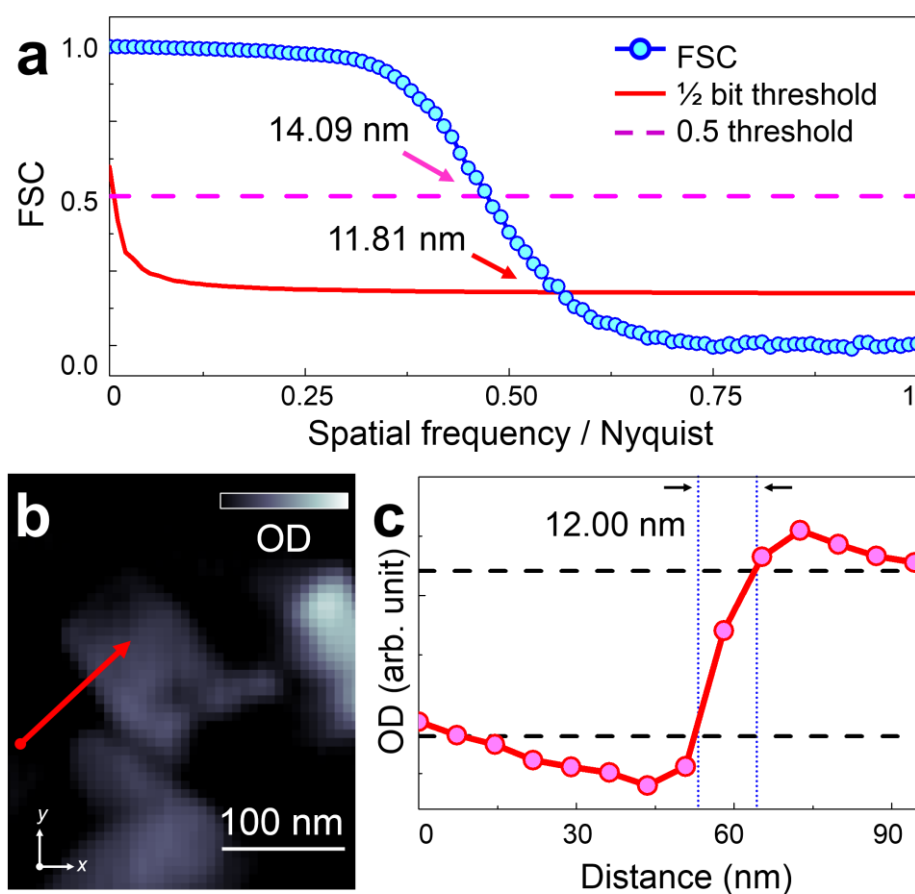


**Figure S7.** Representative cross-section of the tomogram at 708.2 **(a)** and 710.2 eV **(b)** along the low-resolution plane ( $xz$  plane). The positions of the slices are marked as blue arrows in Fig. 1a. **c, d**, Line profiles indicated by the red arrow in **(a)** and **(b)**, respectively. Black-dashed lines are guides for 10-90% resolution criteria.

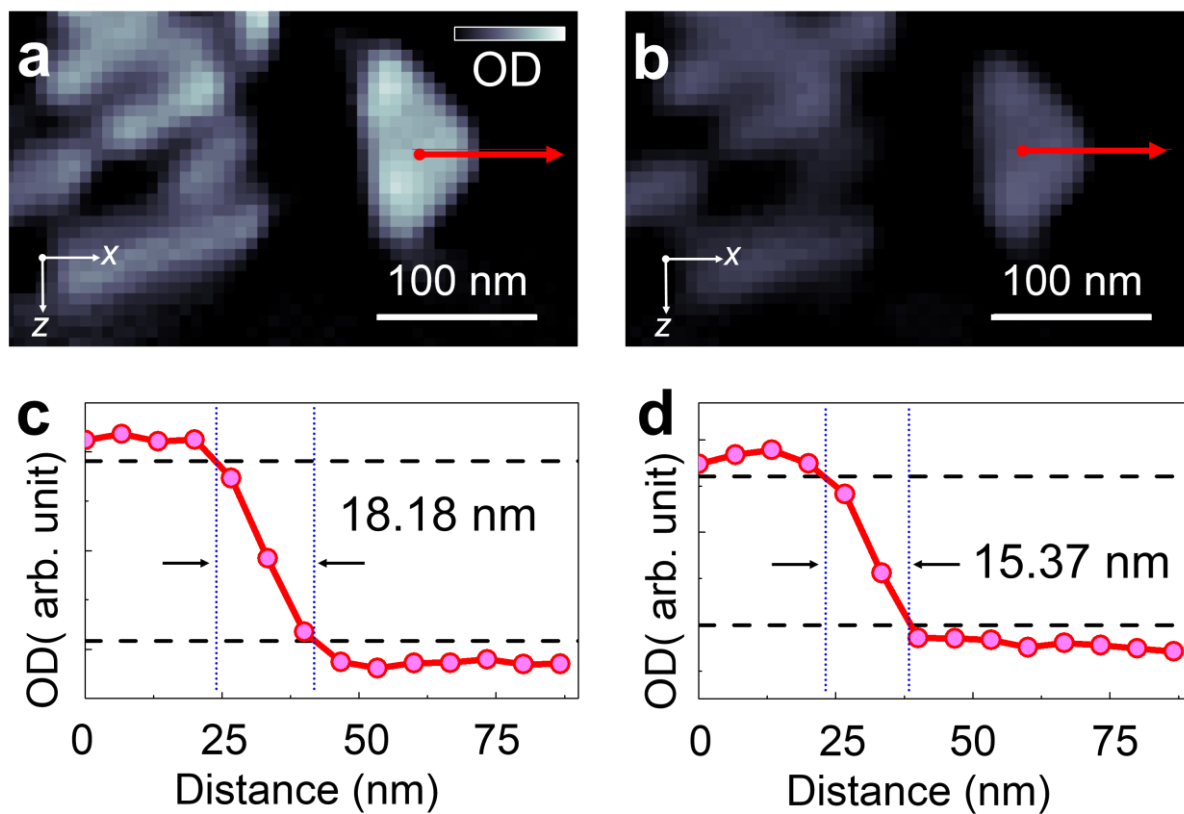


**Figure S8. a**, Correlative distribution plots between the averaged optical density (OD) at two absorption peaks (708.2 and 710.2 eV) and the averaged OD at pre-edge region. To reduce noise in low contrast images at pre-edge region, three OD images (at 700.0, 702.7, and 705.2 eV) are averaged. The linear relation of correlative OD distribution is defined as a red solid line.

**b**, OD ratio map between the averaged OD at two absorption peaks and the averaged OD at pre-edge region.

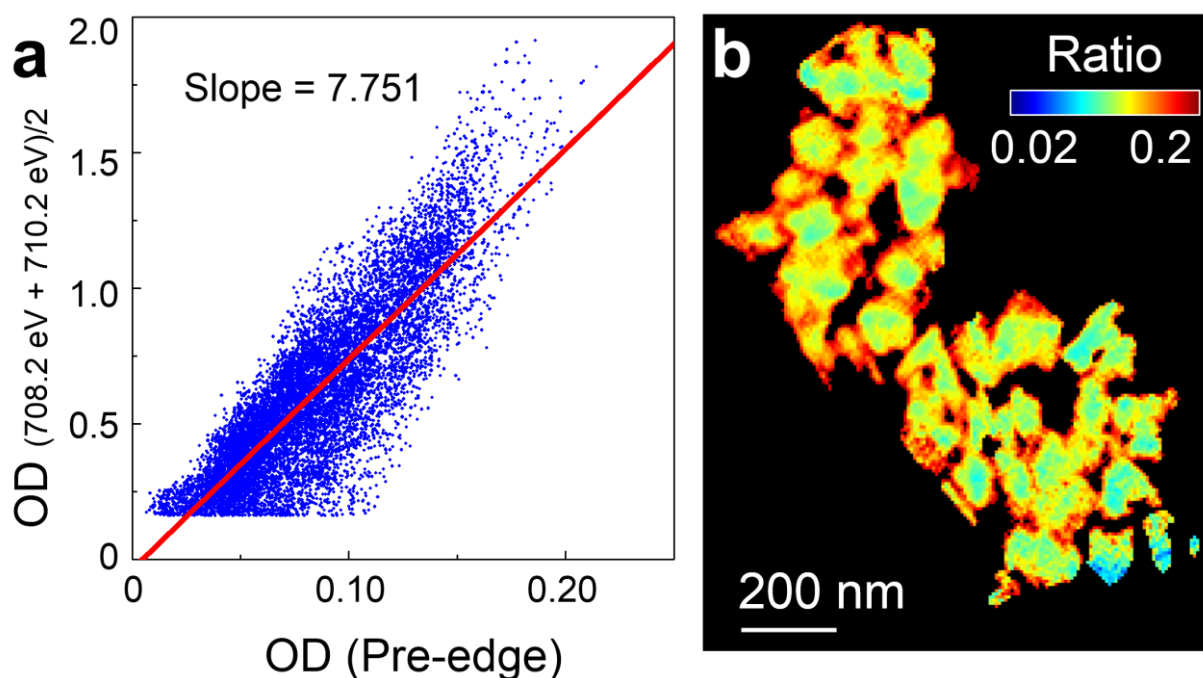




**Figure S9.** **a**, Two dimensional (2D) chemical phase maps obtained by linear combination (LC) fits of XAS data at each pixel. The presence of the  $\text{Li}_\alpha\text{FePO}_4$  (LFP) and  $\text{Li}_\beta\text{FePO}_4$  (FP) were assigned colors red and blue, respectively. The brightness indicates relative sample thickness along X-ray path. **b**, *R*-factor maps depicting the statistical quality of the single pixel fits in (**a**). **c**, Selected XAS spectra extracted from the marked positions in (**a**), and results of LC fits with standard spectra from  $\text{LiFePO}_4$  (LFP) and  $\text{FePO}_4$  (FP). The residue is defined by the difference between XAS data and fit results.

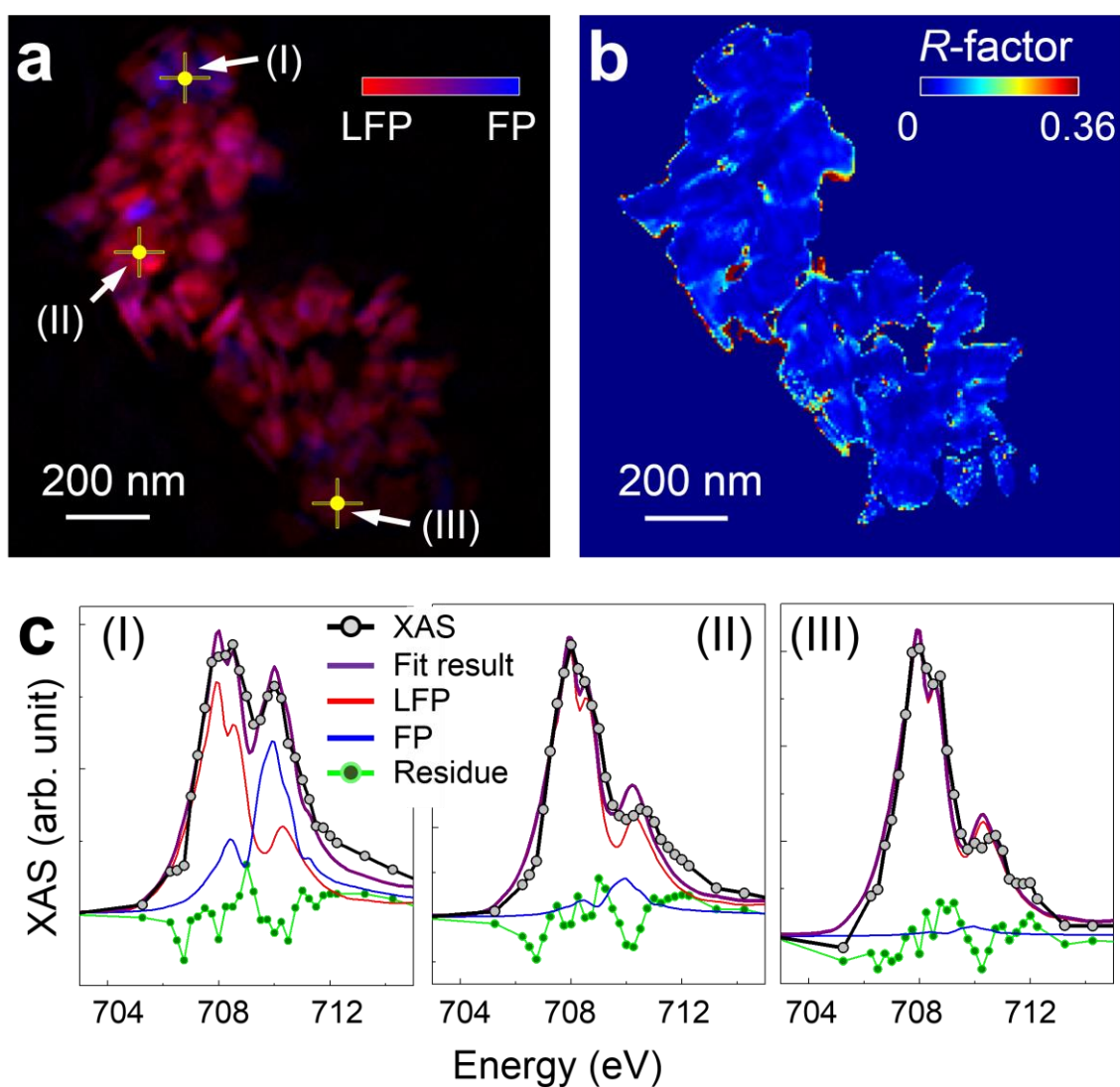




**Figure S10.** Two dimensional (2D) chemical phase maps from different methods; (a) linear combination (LC) fits of full XAS data; (b) the quantitative analysis with two optical density (OD) images at 708.2 and 710.2 eV; (c) the quantitative analysis with two OD images, which are 2D projections of three dimensional (3D) volume at 708.2 and 710.2 eV. The presence of the  $\text{Li}_\alpha\text{FePO}_4$  (LFP) and  $\text{Li}_\beta\text{FePO}_4$  (FP) were assigned colors red and blue, respectively. The brightness indicates relative sample thickness along X-ray path. d, e, f, heat map of chemical distributions, corresponding to the chemical maps in (a), (b), and (c), respectively. Here, the color contrast scales with the ratio of LFP contents in each pixel.

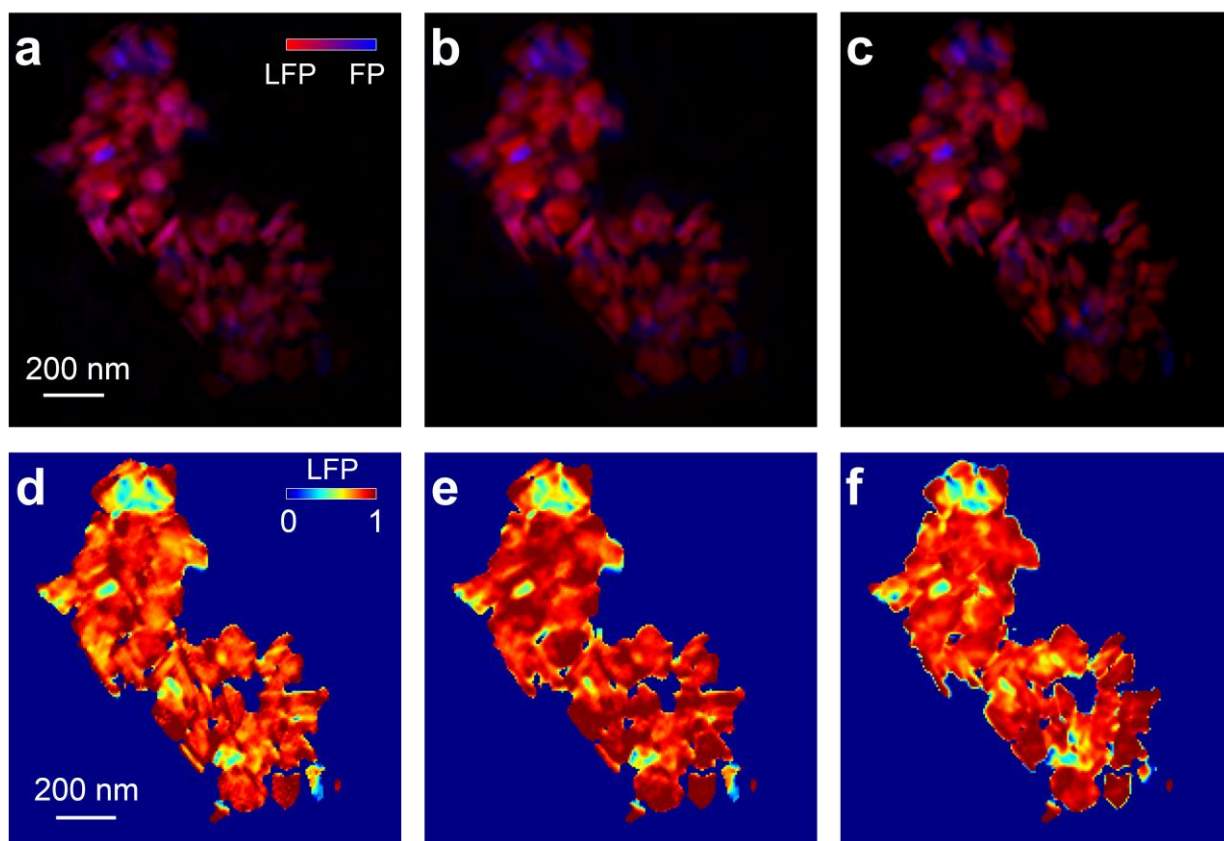


**Figure S11.** Segmentation of two dimensional (2D) chemical phases with 30% threshold. The red, green, and blue areas indicate LFP-rich ( $>70\%$   $\text{Li}_\alpha\text{FePO}_4$ ,  $\alpha \geq 0.9$ ), FP-rich ( $>70\%$   $\text{Li}_\beta\text{FePO}_4$ ,  $\beta < 0.1$ ), and Mixed (30-70%  $\text{Li}_\alpha\text{FePO}_4$ , the rest being  $\text{Li}_\beta\text{FePO}_4$ ) domains, respectively. Each 2D chemical phase map was obtained by different methods; **(a)** linear combination (LC) fits of full XAS data (indexed as 2D-full); **(b)** the quantitative analysis with two optical density (OD) images at 708.2 and 710.2 eV (indexed as 2D-2E); **(c)** the quantitative analysis with two OD images, which are 2D projections of three dimensional (3D) volumes at 708.2 and 710.2 eV (indexed as 3D-2E). **d**, Percentage of bad pixels which have mismatched chemical segments between **(a)** and **(b)** (red solid line with scatter) or **(a)** and **(c)** (blue solid line with scatter) according to the segmentation threshold ( $X$ ).

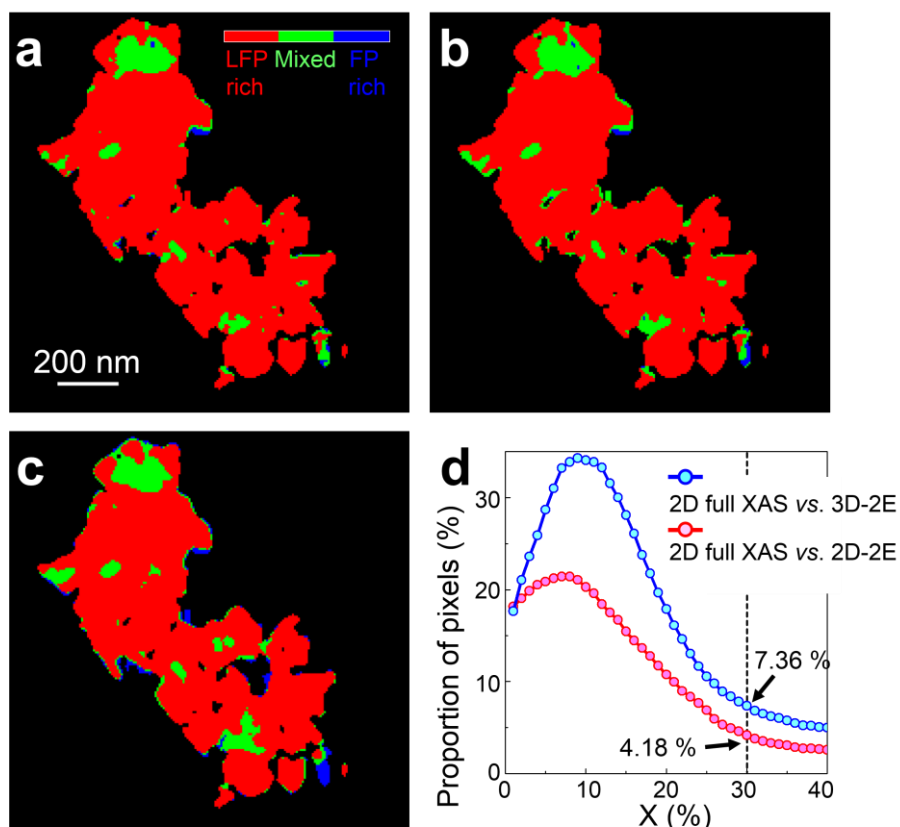
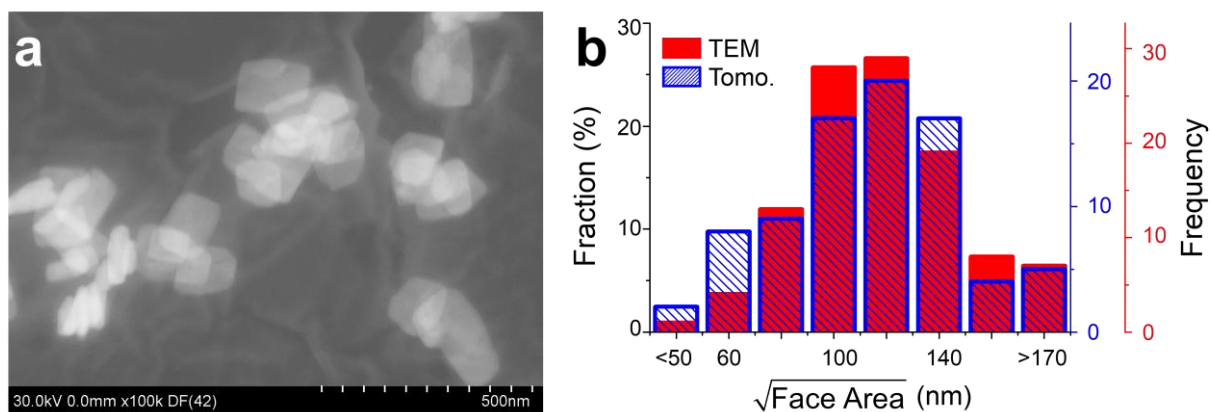


**Figure S12. a,** Representative dark-field transmission electron microscopy (DF-TEM) image of pristine  $\text{LiFePO}_4$ . **b,** Histogram plot of square root of the facet areas. The total number of observed particles are 109 and 83 from the multiple TEM images (red solid bar) and the tomogram (blue hatched bar), respectively.



## Supplementary References

- 1 Deng, J. *et al.* Simultaneous cryo X-ray ptychographic and fluorescence microscopy of green algae. *Proc. Natl. Acad. Sci. USA* **112**, 2314-2319 (2015).
- 2 Crowther, R. A., DeRosier, D. J. & Klug, A. The Reconstruction of a Three-Dimensional Structure from Projections and its Application to Electron Microscopy. *Proc. R. Soc. Lond. A* **317**, 319-340 (1970).
- 3 Shapiro, D. A. *et al.* Chemical composition mapping with nanometre resolution by soft X-ray microscopy. *Nature Photon.* **8**, 765–769 (2014).
- 4 Yu, Y.-S. *et al.* Dependence on crystal size of the nanoscale chemical phase distribution and fracture in  $\text{Li}_x\text{FePO}_4$ . *Nano Lett.* **15**, 4282-4288 (2015).
- 5 Meyer, F. Topographic distance and watershed lines. *Signal Processing* **38**, 113-125 (1994).